Journal of The Electrochemical Society, **156** (4) G23-G27 (2009)
0013-4651/2009/156(4)/G23/5/$23.00 © The Electrochemical Society

High-Performance Metal-Insulator-Metal Capacitor Using Quality Properties of High-κ TiPrO Dielectric

Chingchien Huang,[a,b,z] Chun-Hu Cheng,[b] Ko-Tao Lee,[c,*] and Bo-Heng Liou[d]

[a]*Department of Electrical Engineering and* [b]*Department of Mechanical Engineering, National Chiao-Tung University, Hsinchu, Taiwan*
[c]*Institute of Electronics Engineering, National Tsing Hua University, Hsinchu, Taiwan*
[d]*Instrument Technology Research Center, National Applied Research Laboratories, Hsinchu, Taiwan*

In this paper, we demonstrate excellent material characteristics of TiPrO and high-density $Ti_xPr_{1-x}O$ ($x \approx 0.67$) metal-insulator-metal (MIM) capacitors using high-work-function (~5.3 eV) Ir top electrode. Low leakage current of 7×10^{-9} A/cm^2 at −1 V and high 16 fF/μm^2 capacitance density are achieved for 400°C anneal TiPrO, which also meets the International Technology Roadmap for Semiconductors goals (at year 2018) of 10 fF/μm^2 density and $J/(CV) < 7$ fA/(pF*V*). Furthermore, the improved high 20 fF/μm^2 capacitance density TiPrO MIM was obtained at a higher anneal temperature, where a low leakage current of 1.2×10^{-7} A/cm^2 was measured at −1 V. These good performances indicate that TiPrO MIM is suitable for analog/radio frequency integrated circuits.
 [DOI: 10.1149/1.3073549]

Manuscript submitted July 29, 2008; revised manuscript received December 29, 2008. Published January 30, 2009.

The technology evolution for metal-insulator-metal (MIM) capacitors[1-16] requires higher capacitance density with low leakage current at the evaluating temperature.[17] Besides, the MIM capacitors are also used for analog/radio frequency (rf) integrated circuits (ICs) and dynamic random access memory (DRAM) technology. Low voltage- or temperature-dependence of capacitance is also needed for the multifunctional system-on-chip applications. Because the capacitance density equals $\varepsilon_0\kappa/t_\kappa$, the only method for higher density, without increasing unwanted leakage current by decreasing dielectric thickness (t_κ), is to use higher dielectric constant dielectric (κ) materials. Thus, the MIM capacitors are continuously integrated with higher κ dielectrics from Al_2O_3,[3] HfO_2–Al_2O_3,[9] ZrO_2, TiTaO,[13] TiHfO,[15] and TiNiO.[16] One major drawback for a higher-κ MIM device is the large leakage current due to low conduction-band offset (ΔE_C) at evaluated temperature that leaks out the stored charge in capacitor ($Q = CV$). However, increasing dielectric constant (κ) usually leads to decreasing ΔE_C relating to electrode. This is also the challenge of flash memory but unavoidable during IC operation due to large circuit density and high dc power dispassion from leakage current. A possible solution is using high-bandgap (E_G) dielectric to form the laminate[9] or multilayer structure,[10] but the overall κ value and voltage coefficient of capacitance (VCC) are largely degraded. Pr_2O_3 is an attractive rare-earth metal oxide with many merits such as large conduction-band offset ($\Delta E_C \approx 1$ eV),[18] moderate dielectric constant ($\kappa \approx 15$), and large bandgap ($E_G \approx 4$ eV).[18] Furthermore, significantly larger Gibbs free energy of Pr_2O_3 (+106 kcal/mol)[19-21] in contact with silicon than that of TiO_2 (+7.5 kcal/mol), Ta_2O_5 (−52 kcal/mol), HfO_2 (+47 kcal/mol), and NiO (−51.4 kcal/mol) can avoid metal/oxide interdiffusion or chemical reaction caused by oxygen exchange, which not only reduces the interfacial layer between the dielectric layer and bottom electrode but also creates excellent thermal stability. Combining the above advantages of high-κ Pr_2O_3 with the high dielectric constant of TiO_2 (~60), mixed TiPrO dielectric overcomes the issue of leakage current without scarifying capacitance density.

In this paper, we report Ir/TiPrO/TaN capacitors with a capacitance density of 16 fF/μm^2 and further improved capacitance density of 20 fF/μm^2 using a higher annealing temperature. High-κ values of 26–32 are obtained in this work by using mixed $Ti_xPr_{1-x}O$ ($x \approx 0.67$). By using high-κ TiPrO with a ratio of Ti to Pr of 2:1 and high work function electrode Ir, we can achieve a high capacitance density of 16–20 fF/μm^2 and a low leakage current of 7×10^{-9} to 1.2×10^{-7} A/cm^2 at 25°C at −1 V, small quadratic VCC (α) of 1720–2174 ppm/V^2, and small time coefficient of capacity (TCC) of 532–758 ppm/°C. The lower leakage shows improved quadratic VCC (α) and TCC, which are important for analog/rf functions. The device shows large orders of magnitude lower thermal leakage at 25 and 125°C at −1 V than that of TiTaO[13] and TiNiO[16] MIM capacitors at comparable capacitance density. Such good device integrity is due to the mixed high-κ TiPrO ($\kappa \approx 28$–36) with larger bandgap ($E_G \approx 4$ eV), larger high-κ/Si conduction-band discontinuity ($\Delta E_C \approx 1$ eV), and larger Gibbs free energy (+106 kcal/mol) of Pr_2O_3.

Experimental

After depositing 2 μm SiO_2 on a Si wafer, the lower capacitor electrode was formed using PVD-deposited TaN/Ta bilayers. The Ta was used to reduce the series resistance, and the TaN served as a barrier layer between the high-κ TiPrO and the Ta electrode. The TaN was treated by NH_3 plasma nitridation at 100 W to improve the bottom interface. The TaN layer with NH_3 surface nitridation[22,23] can improve electrode stability and prevent capacitance-effective thickness degradation by forming interfacial TaON during postdeposition anneal (PDA). Then, 16 nm thick $Ti_xPr_{1-x}O$ ($x \approx 0.67$) dielectric was deposited on the TaN/Ta electrode by the dual E-gun evaporation system with separated TiO_2 and Pr_2O_3 targets. The deposition rates of the two targets were controlled as 1:3 (Pr_2O_3:TiO_2). Then, the dielectric films were followed by 400 and 430°C oxidation and annealing steps, respectively, to reduce the leakage current. Finally, Ir was deposited and patterned to form the top capacitor electrode. The fabricated devices were characterized by capacitance–voltage (*C-V*) and current density–voltage (*J-V*) measurements using an HP4155B semiconductor parameter analyzer and an HP4284A precision LCR meter.

Results and Discussion

Figure 1 shows the *C-V* characteristics of Ir/TiPrO/TaN capacitors, which were processed differently. The capacitance density increased from 16 to 20 fF/μm^2 with increasing O_2 PDA temperature from 400 to 430°C. In Fig. 2a and b, we perform the *J-V* characteristics of the TiPrO MIM capacitors with capacitance density of 16 and 20 fF/μm^2, respectively, measured at 25 and 125°C. Good *J-V* and *C-V* characteristics are obtained with the use of high-work-function top-electrode Ir (~5.27 eV) and nitrogen plasma (N^+) treatment on bottom-electrode TaN. The nitrogen plasma (N^+) treatment reduces the interfacial layer growing between the bottom electrode TaN and TiPrO layer during oxygen annealing.[22,23] The TiPrO MIM with a capacitance density of 16 fF/μm^2 achieves the International Technology Roadmap for Semiconductors (ITRS) goals (at

* Electrochemical Society Student Member.
z E-mail: carrson.huang@hotmail.com

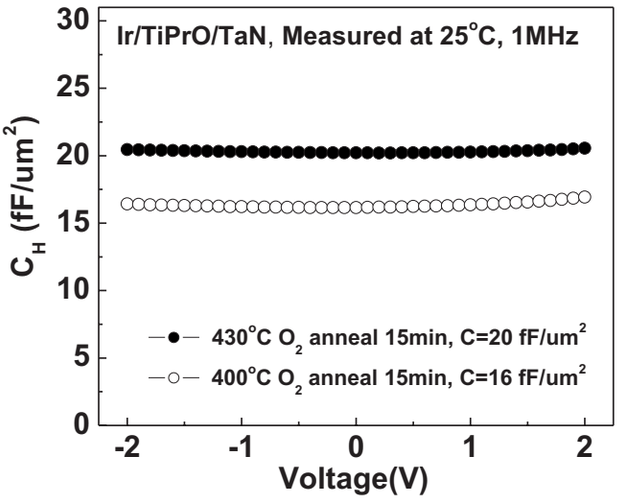

Figure 1. *C-V* characteristics of Ir/TiPrO/TaN capacitors with different annealing temperatures measured at 1 MHz.

year 2018)[17] of 10 fF/μm^2 density and $J/(CV) < 7$ fA/(pF*V*). This result indicates that TiPrO is a potential material candidate for future electrical device application.

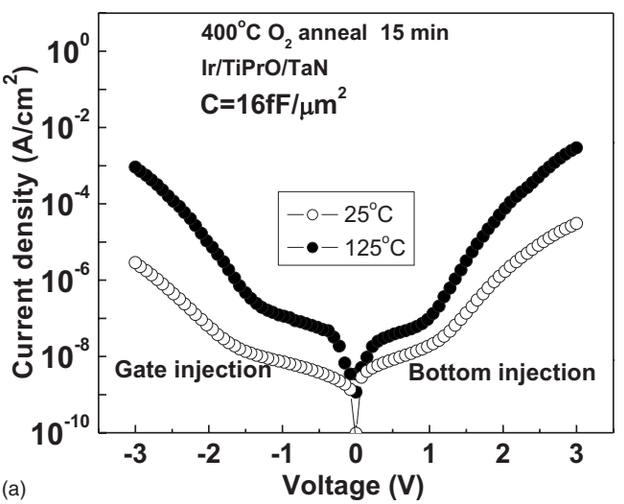

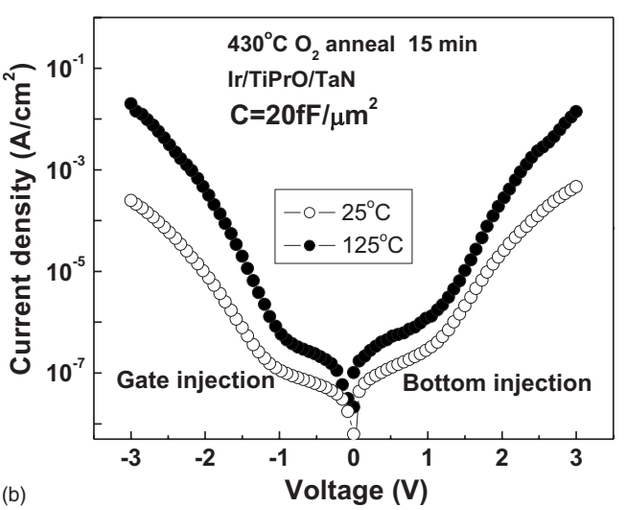

Figure 2. *J-V* characteristics of Ir/TiPrO/TaN capacitors with different capacitance densities (16 and 20 fF/μm^2) measured at 25 and 125°C, respectively.

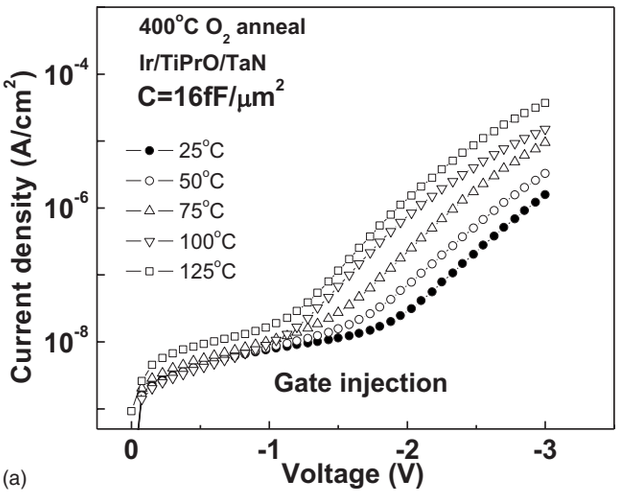

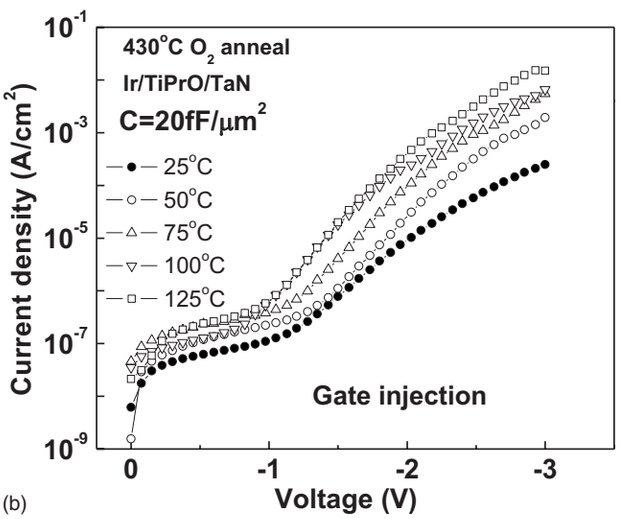

Figure 3. *J-V* characteristics of Ir/TiPrO/TaN capacitors for capacitance density with (a) 16 fF/μm^2 and (b) 20 fF/μm^2 measured from 25 to 125°C, respectively.

To further evaluate the device performance, Fig. 3a and b show the temperature-dependent *J-V* characteristics of TiPrO MIM capacitors at capacitance densities of 16 and 20 fF/μm^2, respectively. The leakage current increases rapidly with increasing temperature; however, the high-temperature operation is unavoidable for modern high-performance IC due to increasing power consumption. In addition, the unwanted interfacial layer between the bottom electrode and high-κ dielectric layer would lead to surface roughness between them. The interfacial layer makes the thermal leakage current of the electron bottom injection (voltage = 0–3 V) slightly larger than the leakage of the electron gate injection (voltage = 0 to − 3 V), which can be observed in Fig. 2. Thus, we only perform the *J-V* characteristics under reverse bias in Fig. 3.

The examination of device performance with comparable capacitance density at 25°C is performed in Fig. 4. From Fig. 4, we can see that the leakage current of TiPrO MIM is significantly lower than TiO_2 MIM, TiTaO MIM, and TiNiO MIM at a comparable capacitance density. The lower leakage current of TiPrO MIM is due to the higher ΔE_C between metal and high-κ TiPrO interface, higher bandgap of high-κ TiPrO, and larger Gibbs free energy of Pr_2O_3, which reduce the leakage current exponentially. We also plot the

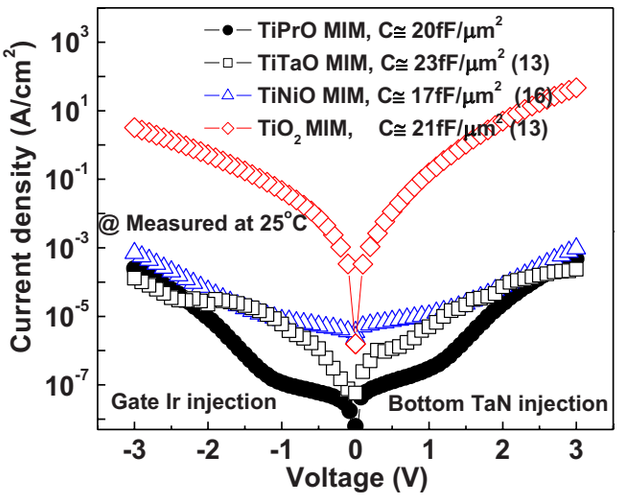

Figure 4. (Color online) The comparisons of *J-V* for different high-κ material capacitors at comparable capacitance density. The leakage current of TiPrO MIM is significantly lower than TiO_2 and TiTaO and TiNiO MIM.

ln(*J*) vs $E^{1/2}$ relation in Fig. 5. The temperature-dependent leakage current in MIM is typically governed by Schottky emission (SE) or Frenkel–Poole (FP) as

$$J \propto \exp\left(\frac{\gamma E^{1/2} - V_b}{kT}\right) \quad [1]$$

$$\gamma = \left(\frac{e^3}{\eta\pi\varepsilon_0 K_\infty}\right)^{1/2} \quad [2]$$

η is equal to 1 or 4 for the FP or SE case, and K_∞ is the high-frequency dielectric constant ($=n^2$). The refractive index $n = 2.3$ for $Ti_xPr_{1-x}O$ ($x \approx 0.67$) is reasonable by linear interpolation of the reported 2.57 for TiO_2 and 1.75 for Pr_2O_3. From Fig. 5a and b, the leakage at 25°C from the Ir top electrode on TiPrO/TaN is ruled by SE at low field and FP at high field by trap-conduction. In addition, the leakage at 125°C is also dominated by SE at low field and FP at

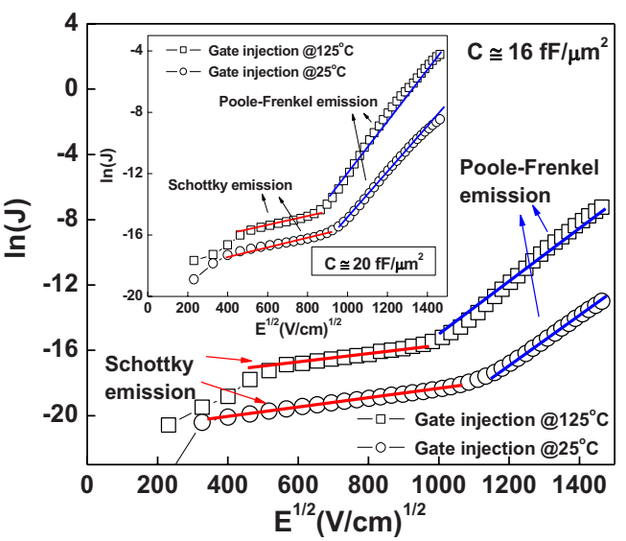

Figure 5. (Color online) Plot of ln(*J*) vs $E^{1/2}$ under electron injection from top electrode for Ir/TiPrO/TaN capacitors with capacitance density of 16 fF/μm²; capacitance density of 20 fF/μm² is shown in the insert. The SE emission fitting at low electric field and the FP emission fitting at high electric field are measured at 25 and 125°C, respectively.

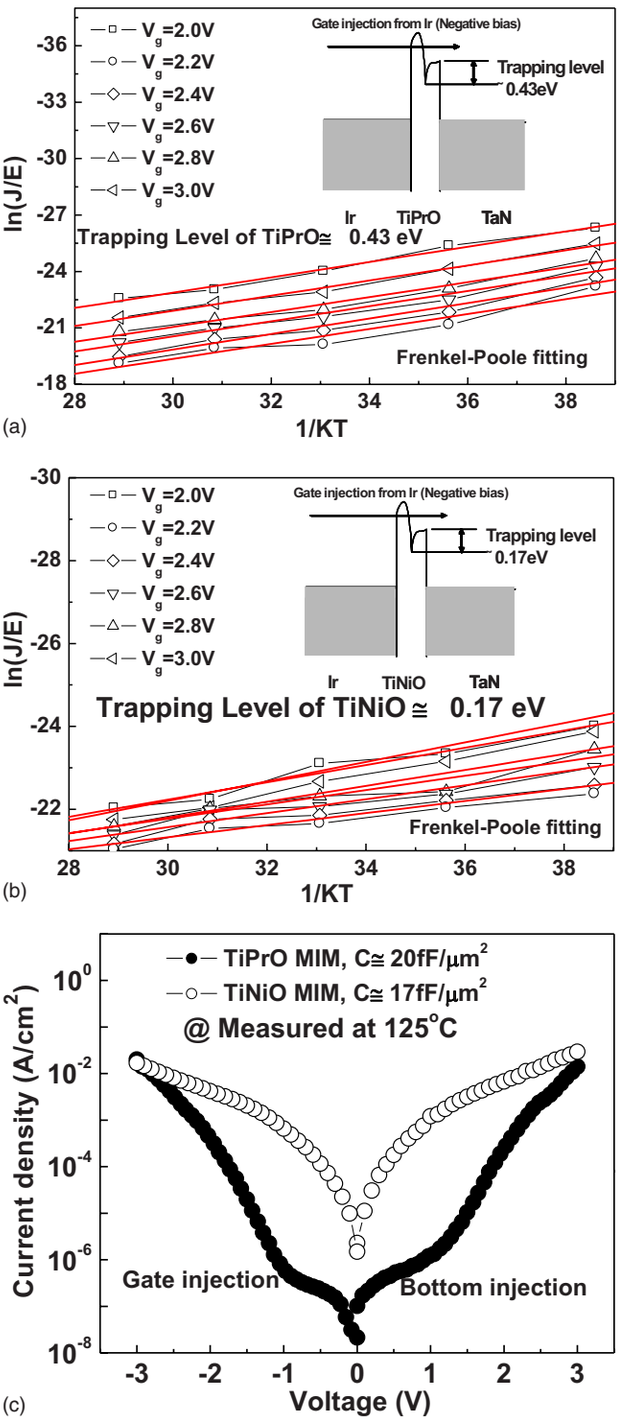

Figure 6. (Color online) The FP conduction fitting at high field for (a) Ir/TiPrO/TaN capacitor and (b) Ir/TiPrO/TaN capacitor, and (c) the leakage current measured at 125°C for Ir/TiPrO/TaN and Ir/TiN*i*O/TaN MIM..

high field. This result would be due to the large ΔE_C and bandgap of TiPrO and the larger energy barrier ϕ_b of Ir electrode. The different slopes γ for the SE and FP cases arise from the different energy barriers V_b corresponding to the work function of the metal-electrode/dielectric in the SE case or the trap energy level in the dielectric for the FP case. The fits to the experimental data give a slope of 1.56 or 3.14×10^{-5} eV $(m/V)^{1/2}$ for the SE or FP mechanisms, respectively,[23] by using $n = 2.3$ for TiPrO in the above equations.

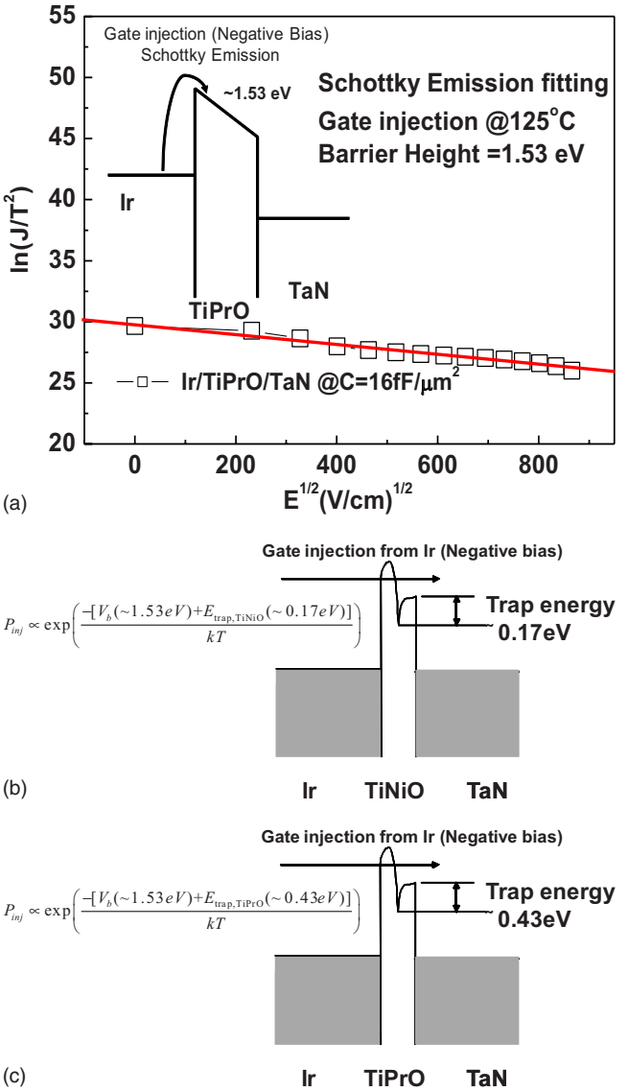

Figure 7. (Color online) (a) The SE emission fitting of Ir/TiPrO/TaN capacitors at low electric field. (b and c) Illustration for electron injection from Ir top electrode to the trap states present at TiNiO dielectric and TiPrO dielectric in MIM capacitor, respectively. The trapping-level difference between TiPrO and TiNiO dielectric (ΔE_{trap}) makes a great impact on the electron injection probability (P_{inj}).

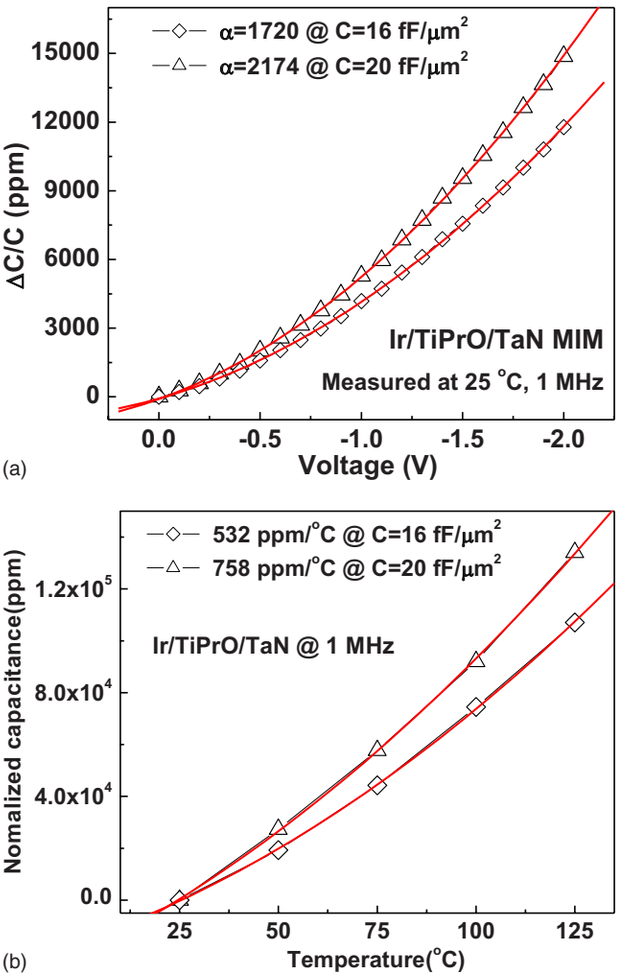

Figure 8. (Color online) (a) $\Delta C/C$-V characteristics of Ir/TiPrO/TaN capacitors for different capacitance density. (b) The temperature-dependent normalized capacitance for Ir/TiPrO/TaN capacitors for different capacitance density.

Because the conduction mechanism at high electric field for Ir electrode on TiPrO is governed by FP emission, we plotted the $\ln(J/E)$-$1/KT$ relation of TiPrO in Fig. 6a to extract the trapping level. The larger Gibbs free energy of Pr_2O_3 (+106 kcal/mol) contacted with silicon avoids metal/oxide interdiffusion. Besides, the binding energy between praseodymium and oxygen (928–970 eV)[24] is significantly larger than the binding energy between nickel and oxygen (855–861 eV)[25] and that between tantalum and oxygen (~530 eV).[26] Both reasons indicate that the interfacial trap density of TiPrO (between dielectric and electrode) would be smaller than that of other dielectrics, such as TiTaO and TiNiO. Thus, the trapping level in the TiPrO dielectric would be larger than TiTaO (~0.3 eV)[13] and TiNiO.[16] For illustration, we also plot this relation of TiNiO MIM in Fig. 6b. Compared with Fig. 6a and b, the trapping level of TiPrO of about 0.43 eV is remarkably larger than the trapping level of TiNiO of about 0.17 eV. This result also explains why TiPrO MIM can achieve nearly 2.5 orders of magnitude lower leakage current at −1 V at 125°C than TiNiO MIM, which is shown in Fig. 6c. In Fig. 7a, the SE barrier height (V_b) at 125°C was extracted from the $\ln(J/T^2) - E^{1/2}$ plot. The value for V_b is 1.71 eV for the TiPrO device at 125°C with Ir top electrode. This result also attests to the fact that the low leakage current can be achieved using our device. Additionally, in Fig. 7b and c, we illustrate the electron injection from Ir top electrode to the trap states present at TiPrO dielectric and TiNiO dielectric in MIM capacitor, respectively. The trapping-level difference between TiPrO and TiNiO dielectric ($\Delta E_{trap} \approx 0.23$ eV) has a significant impact on the electron injection probability (P_{inj}). The 0.23 eV difference of ΔE_{trap} results in 10^{-3} order reduction of P_{inj} for TiPrO MIM compared to that of the TiNiO MIM capacitor. The relation between P_{inj} and trapping level is shown in the following equation[27,28]

$$P_{in} \propto \exp\left[\frac{-(V_b + E_{trap,dielectric})}{kT}\right] \quad [3]$$

VCCs are important parameters for MIM capacitor applications and can be obtained by fitting the measured data with a second-order polynomial equation of $C(V) = C(\alpha V^2 + \beta V + 1)$, where C is the zero-biased capacitance and α and β represent the quadratic and linear voltage coefficients of capacitance, respectively. Figure 8a shows $\Delta C/C$-V characteristics of Ir/TiPrO/TaN capacitors fitted by the above-mentioned equation. The lower leakage using high ϕ_m (Ir) also improves $\Delta C/C$ and VCC α due to the trap-related

Table I. Comparison of important device data for MIM Ir/TiPrO/TaN capacitor with various high-κ dielectrics and work-function metals.

	ITRS at 2018	Tb–HfO_2 (Ref. 6)	Al_2O_3–HfO_2 (Ref. 9)	Nb_2O_5 (Ref. 12)	TiTaO (Ref. 13)	TiNiO (Ref. 16)	This work	
Process Temperature (°C)	—	420	420	420	400	400	400	430
Top metal	—	Ta	TaN	Ta	Ir (5.3 eV)	Ni (5.1 eV)	Ir* (5.3 eV)	Ir* (5.3 eV)
Lower metal	—	TaN	TaN	Ta	TaN	TaN	TaN	TaN
C density (fF/μm^2)	10	13.3	12.8	17.6	23	17.1	16	20
J (A/cm^2) at 25°C	—	1×10^{-7} (2 V)	8×10^{-9} (2 V)	7×10^{-7} (1 V) 8×10^{-7} (2 V)	2×10^{-6} (1 V) 2×10^{-5} (2 V)	7.7×10^{-6} (1 V) 5.6×10^{-5} (2 V)	7×10^{-9} (1 V) 1.1×10^{-7} (2 V)	1.2×10^{-7} (1 V) 7.4×10^{-6} (2 V)
J (A/cm^2) at 125°C	—	2×10^{-7} (2 V)	6×10^{-9} (1 V) 5×10^{-8} (2 V)	4×10^{-7} (1 V) 1×10^{-5} (2 V)	—	—	3.6×10^{-7} (1 V) 7.2×10^{-6} (2 V)	5.8×10^{-7} (1 V) 3.8×10^{-4} (2 V)
J/(CV) (fA/[pFV])	<7	37.9 at 2 V	3.1 at 2 V	14.5 at 1.5 V	870 at 1 V	4530 at 1 V	3.45 at 1 V	45 at 1 V

mechanism.[3,4,7,8] Because linear VCC β can be cancelled by circuit design,[29] α is important for analog/rf functions, and it is strongly dependent on electric field and dielectric physical thickness. To the best of our knowledge, the MIM capacitor with combined higher ϕ_m and higher κ dielectric is the only method to achieve lower thermal leakage and better VCC α simultaneously without scarifying capacitance density in a multilayer or laminate structure. Figure 8b shows the normalized TCC of MIM capacitor for capacitance density of 16 and 20 fF/μm^2, respectively. We find that the TCC showed an increase with the increase in measured temperature.[14]

Amorphous dielectrics like TiPrO have some advantages over crystalline materials, including low processing thermal budget, conventional electrode, high uniformity, and scalability to thin layers, which is suitable for back end of line and manufacture. Table I summarizes important device data for MIM capacitors with various high-κ dielectrics and work-function metals. The thermal leakage decreases largely with increasing ϕ_m of metal electrode from TaN to Ir. High 16–20 fF/μm^2 density, reasonable quadratic VCC α of 1702–2174 ppm/V^2, and low 7×10^{-9}–1.2×10^{-7} A/cm^2 leakage current at 25°C at −1 V are simultaneously measured in Ir/TiPrO/TaN devices, which are comparable with or better than the best reported data in literature.[17] In a word, amorphous dielectric TiHfO shows good thermal stability, leakage current, and scalability to thin layers. TiPrO is also a better amorphous dielectric material than TiO_2, TiTaO, and TiNiO.

Conclusions

Due to large conduction-band offset (~1 eV), large bandgap (4 eV), large Gibbs free energy (~106 kcal/mol) of Pr_2O_3, large binding energy of Pr_2O_3 (928–970 eV), and high dielectric constant (~60) of TiO_2, the mixed high-κ TiPrO is a potential material candidate for electronic devices. Dielectric material TiPrO shows excellent amorphous material properties and gives enough high-κ value (κ ≈ 28–36). By applying the good properties to our MIM device, the device not only shows apparently lower thermal leakage than other dielectric MIM at comparable capacitance density but also meets the ITRS requirement. Such good device integrity indicates that TiPrO dielectric is a promising dielectric material for analog/rf ICs and DRAM applications.

Acknowledgments

The authors acknowledge a great appreciation to Dr. Chun-Hu Cheng at National Chiao Tung University for his inspiring discussion and suggestions and to Kao-Tao Lee and Bo-Heng Liou for assistance in running the relative experiments.

References

1. C.-M. Hung, Y.-C. Ho, I. C. Wu, and K. O, *IEEE MTT-S Int. Microwave Symp. Dig.*, **46**, 505 (1998).
2. J. A. Babcock, S. G. Balster, A. Pinto, C. Dirnecker, P. Steinmann, R. Jumpertz, and B. E. Kareh, *IEEE Electron Device Lett.*, **22**, 230 (2001).
3. S. B. Chen, J. H. Lai, K. T. Chan, A. Chin, J. C. Hsieh, and J. Liu, *IEEE Electron Device Lett.*, **23**, 203 (2002).
4. C. Zhu, H. Hu, X. Yu, S. J. Kim, A. Chin, M. F. Li, B. J. Cho, and D. L. Kwong, *Tech. Dig. - Int. Electron Devices Meet.*, **2003**, 879.
5. X. Yu, C. Zhu, H. Hu, A. Chin, M. F. Li, B. J. Cho, D.-L. Kwong, P. D. Foo, and M. B. Yu, *IEEE Electron Device Lett.*, **24**, 63 (2003).
6. S. J. Kim, B. J. Cho, M.-F. Li, C. Zhu, A. Chin, and D. L. Kwong, *Dig. Tech. Pap. - Symp. VLSI Technol.*, **2003**, 77.
7. C. H. Huang, M. Y. Yang, A. Chin, C. X. Zhu, M. F. Li, and D. L. Kwong, *IEEE MTT-S Int. Microwave Symp. Dig.*, **1**, 507 (2003).
8. M. Y. Yang, C. H. Huang, A. Chin, C. Zhu, B. J. Cho, M. F. Li, and D. L. Kwong, *IEEE Microw. Wirel. Compon. Lett.*, **13**, 431 (2003).
9. H. Hu, S. J. Ding, H. F. Lim, C. Zhu, M. F. Li, S. J. Kim, X. F. Yu, J. H. Chen, Y. F. Yong, B. J. Cho, et al., *Tech. Dig. - Int. Electron Devices Meet.*, **2003**, 379.
10. Y. K. Jeong, S. J. Won, D. K. Jwon, M. W. Song, W. H. Kim, O. H. Park, J. H. Jeong, H. S. Oh, H. K. Kang, and K. P. Suh, *Dig. Tech. Pap. - Symp. VLSI Technol.*, **2004**, 222.
11. C. H. Huang, D. S. Yu, A. Chin, W. J. Chen, C. X. Zhu, M. F. Li, B. J. Cho, and D. L. Kwong, *Tech. Dig. - Int. Electron Devices Meet.*, **2003**, 319.
12. S. J. Kim, B. J. Cho, M. B. Yu, M.-F. Li, Y.-Z. Xiong, C. Zhu, A. Chin, and D. L. Kwong, *Dig. Tech. Pap. - Symp. VLSI Technol.*, **2005**, 56.
13. K. C. Chiang, A. Chin, C. H. Lai, W. J. Chen, C. F. Cheng, B. F. Hung, and C. C. Liao, *Dig. Tech. Pap. - Symp. VLSI Technol.*, **2005**, 62.
14. K. C. Chiang, C. C. Huang, A. Chin, W. J. Chen, S. P. McAlister, H. F. Chiu, J. R. Chen, and C. C. Chi, *IEEE Electron Device Lett.*, **26**, 504 (2005).
15. C. H. Cheng, K.-C. Chiang, H.-C. Pan, C.-N. Hsiao, C.-P. Chou, S. P. Mcalister, and A. Chin, *Jpn. J. Appl. Phys., Part 1*, **46**, 7300 (2007).
16. C. C. Huang, C. H. Cheng, A. Chin, and C. P. Chou, *Electrochem. Solid-State Lett.*, **10**, H287 (2007).
17. *The International Technology Roadmap for Semiconductors*: Semicond. Ind. Assoc. (2005).
18. H. J. Osten, E. Bugiel, J. Dabrowski, A. Fissel, T. Guminskaya, J. P. Liu, H. J. Mussig, and P. Zaumseil, in *IEEE IWGI, Tokyo*, pp. 100–106 (2001).
19. K. J. Hubbard and D. G. Schlom, *J. Mater. Res.*, **11**, 2757 (1996).
20. I. Barin and O. Knacke, *Thermochemical Properties of Inorganic Substances*, Springer-Verlag, Berlin (1973).
21. I. Barin, O. Knacke, and O. Kubaschewski, *Thermochemical Properties of Inorganic Substances, Supplement*, Springer-Verlag, Berlin (1977).
22. K. C. Chiang, C. C. Huang, A. Chin, W. J. Chen, H. L. Kao, M. Hong, and J. Kwo, *Dig. Tech. Pap. - Symp. VLSI Technol.*, **2006**, 126.
23. K. C. Chiang, C. C. Huang, A. Chin, G. L. Chen, W. J. Chen, Y. H. Wu, and S. P. McAlister, *IEEE Trans. Electron Devices*, **53**, 2312 (2006).
24. S. Lütkehoff, M. Neumann, and A. Ślebarski, *Phys. Rev. B*, **52**, 13808 (1995).
25. H. M. Meyer III, D. M. Hill, J. H. Weaver, K. C. Goretta, and U. Balachandran, *J. Mater. Res.*, **6**, 270 (1991).
26. E. Atanassova and D. Spassov, in *Proceedings of the 23rd International Conference on Microelectronics*, IEEE, pp. 709–712 (2002).
27. J. M. Frenkel, *Tech. Phys. USSR*, **5**, 685 (1938).
28. S. M. Sze, *J. Appl. Phys.*, **38**, 2951 (1967).
29. K. S. Tan, S. Kiriake, M. de Wit, J. W. Fattaruso, C.-Y. Tsay, W. E. Matthews, and R. K. Hester, *IEEE J. Solid-State Circuits*, **25**, 1318 (1990).